

# On the nature and charge state of the X-Defect, a radiation-induced Silicon defect with field-enhanced charge carrier emission

Niels G. Sorgenfrei<sup>a,b,\*</sup>, Yana Gurinskaya<sup>a</sup>, Anja Himmerlich<sup>a</sup>, Michael Moll<sup>a</sup>, Ulrich Parzefall<sup>b</sup>, Ioana Pintilie<sup>c</sup>, Joern Schwandt<sup>d</sup>

<sup>a</sup>CERN, European Organization for Nuclear Research, Esplanade des Particules 1, Geneva, 1211, Switzerland

<sup>b</sup>Institute of Physics, Albert-Ludwigs-Universitaet Freiburg, Hermann-Herder-Strasse 3, Freiburg im Breisgau, 79104, Germany

<sup>c</sup>National Institute of Materials Physics, Atomistilor 405A, Magurele, 077125, Romania

<sup>d</sup>Institute for Experimental Physics, University of Hamburg, Luruper Chaussee 149, Hamburg, 22761, Germany

## Abstract

The elusive X-Defect, a defect found in low-resistivity *p*-type Silicon after irradiation, observed as a low-temperature shoulder of the B<sub>i</sub>O<sub>i</sub> defect (Boron-interstitial-Oxygen-interstitial complex) in Thermally Stimulated Current (TSC) measurements, was investigated to determine its properties, matching them with those of a previously identified defect. Through a combination of TSC, Deep-Level Transient Spectroscopy (DLTS), Difference-DLTS (DDLTS), numerical simulations of field-enhanced charge carrier emissions in TSC measurements and a comparison to literature, the X-Defect was identified as the singly positively charged Silicon di-vacancy V<sub>2</sub>(+/0). This assignment is supported by an agreement in activation energy, capture cross-section, trap type and charge emission process, as well as simulations comparing the effects of phonon-assisted tunnelling (PAT) and Poole-Frenkel (PF) mechanisms on TSC spectra. DDLTS measurements revealed a quadratic dependence of the activation energy on the electric field strength, confirming PAT as the prevailing mechanism over PF in the case of the radiation-induced X-Defect. Assigning the X-Defect to an electrically neutral defect in the space charge region resolves previous contradictions regarding its deficiency in impacting on the effective doping concentration.

**Keywords:** DLTS, TSC, point defects, *p*-type Silicon, electron irradiation, gamma irradiation, Poole-Frenkel, phonon-assisted tunnelling, field-enhanced emission

## 1. Introduction & History of the X-Defect

Radiation-induced defects in the Silicon lattice can significantly influence detector performance. Energy levels from defects located deep within the bandgap result in increased leakage currents and enhanced carrier trapping, reducing the charge collection efficiency of a Silicon detector. Examples of this are the V<sub>3</sub> (Silicon tri-vacancy) and I<sub>P</sub> (interstitial Phosphorus) point defects [1, 2, 3, 4]. Deactivation of active dopant atoms, as well as the generation of Coulomb centres during irradiation introduces a change in the effective doping concentration  $N_{\text{eff}}$ . Unlike usual trapping

centres, such defects remain charged after ionization at the sensor's operating temperature (usually around  $-20^\circ\text{C}$ ), resulting in altered electric field strengths at a given bias voltage. Key examples for the deactivation of dopants are the VP (Silicon-vacancy-Phosphorus-substitutional complex) and B<sub>i</sub>O<sub>i</sub> (Boron-interstitial-Oxygen-interstitial complex) defects in *n*-type and *p*-type Silicon, respectively [5, 6, 7]. Examples of Coulomb centres, defects with field enhanced emission, generated during irradiation, irrespective of the dopant type and with a strong influence on  $N_{\text{eff}}$  are the BD centres, associated with thermal double donors (TDD2), and the acceptors H116K, H140K and H152K, associated with small vacancies clusters [8, 9, 10]. Importantly, only defects charged in the depletion region can affect  $N_{\text{eff}}$  at the usual operation temperature.

In irradiated low-resistivity *p*-type Silicon, the

\*Corresponding author

Email address: niels.sorgenfrei@cern.ch (Niels G. Sorgenfrei)

most detrimental effect on  $N_{\text{eff}}$  is due to the formation of  $\text{B}_i\text{O}_i$  defects. This is known as the acceptor-removal effect (ARE) and is considered to be the main mechanism behind the gain layer degradation observed in Low Gain Avalanche Detectors (LGADs) [11]. This defect is the result of a Boron dopant atom (acceptor) being knocked-out from its lattice site ( $\text{B}_i$ ), becoming an interstitial and subsequently combining with an interstitial Oxygen ( $\text{O}_i$ ) impurity to form an electrically active defect, the  $\text{B}_i\text{O}_i$ . This defect is a positively charged donor state in Silicon, effectively decreasing  $N_{\text{eff}}$  by double the amount of acceptors (Boron) removed when forming the  $\text{B}_i\text{O}_i$  complex. Various defect-engineering approaches, such as Phosphorus compensation or Carbon co-doping in LGADs, are being tested to improve gain layer longevity [12, 13].

In the context of investigations of the  $\text{B}_i\text{O}_i$  defect in low-resistivity  $p$ -type Silicon, a presumably so-far not observed defect was discovered in Thermally Stimulated Current (TSC) measurements. This defect appeared as a low-temperature shoulder to the  $\text{B}_i\text{O}_i$  peak, see Figure 1, and showed an electric field enhanced emission and a temperature dependence of the carrier (holes) capture process [14, 15, 16, 17]. No defect with such properties was previously reported as being induced by irradiation and it was therefore labelled the X-Defect. Its emission rate, dependent on the electric field strength was tentatively explained by the Poole-Frenkel mechanism [18]. This, however, would imply that the defect must be charged in the depleted region and therefore should impact  $N_{\text{eff}}$  at ambient temperatures. This resulted in a puzzling observation: the change in concentration of the X-Defect did not correlate with the change in the measured  $N_{\text{eff}}$ .

In this article, the X-Defect is further investigated using Deep-Level Transient Spectroscopy (DLTS) and TSC measurements. Electron- and  $\gamma$ -irradiated  $p$ -type Silicon diodes are studied, and simulations of charge carrier emission processes from defects are performed. By comparing the measured characteristics of the X-Defect with defect parameters reported upon in literature, a match of this defect with the singly charged di-vacancy in the donor charge state,  $\text{V}_2(+/0)$ , was found.

This article is a direct follow-up to our previous work [19], in which the identification of the X-Defect as the  $\text{V}_2(+/0)$  was already hypothetically proposed, but could not be verified.

In-depth explanations of the spectroscopic methods TSC and DLTS can be found in Ref. [20] and

the references therein. Since then, the TSC method was further developed both in terms of experimental procedures and methods to analyse the signal for obtaining accurate values for both defect parameters and defect concentrations. Only with these developments it became possible to establish a connection between microscopic and macroscopic properties in irradiated Silicon detectors [16, 21, 22]. The method of the Difference-DLTS measurements will be briefly explained in Section 3.2.1 and is illustrated in Ref. [23].

## 2. Experimental Methods and Materials

Two  $p$ -type epitaxial Silicon pad diodes produced by *CiS Forschungsinstitut für Mikrosensorik GmbH* [24] were investigated. The two diodes differ in their bulk resistivity but are otherwise identical. Both diodes have a thickness of 50  $\mu\text{m}$  and an active pad area (encased by the guard-ring structure) of 6.927  $\text{mm}^2$ . The diode with a nominal resistivity of 10  $\Omega\text{cm}$  was irradiated with 5.5 MeV electrons to a fluence of  $5 \cdot 10^{14} \text{ e}^-/\text{cm}^2$  and has an effective doping concentration  $N_{\text{eff}}$  of  $9.9 \cdot 10^{14} \text{ cm}^{-3}$  after irradiation. The irradiation was carried out at the Belarusian state university in Minsk [25]. The other diode, with a nominal resistivity of 250  $\Omega\text{cm}$ , was irradiated with  $^{60}\text{Co}$ - $\gamma$  to a dose of 2 MGy and has a  $N_{\text{eff}}$  of  $1.3 \cdot 10^{13} \text{ cm}^{-3}$  after irradiation. The irradiation was carried out at the Ruđer Bošković institute in Croatia [26].

The low-resistivity (10  $\Omega\text{cm}$ ) sample was chosen for most of the measurements, as its low resistivity results in stronger electric fields for the same bias voltage, which becomes relevant for the electric field strength dependency measurements presented in Section 3.2.1. It has to be noted that the energy of the electrons used for the irradiation is slightly above the threshold value for producing clustered defects in Silicon [27]. This means that not only point-like defects, but also clustered defects can be created, which may distort peak shapes and activation energies. However, only a minor influence from this effect is expected [27]. In the  $\gamma$ -irradiated sample, only point-like defects are expected. This sample however, has a higher resistivity, resulting in lower electric field strengths. Ideally, low-resistivity  $\gamma$ -irradiated samples would be best suited for this study, but were not available.

The DLTS measurements were performed using the commercial system FT 1030 from PhysTech [28]. The TSC measurements utilised a Keithley 6517A

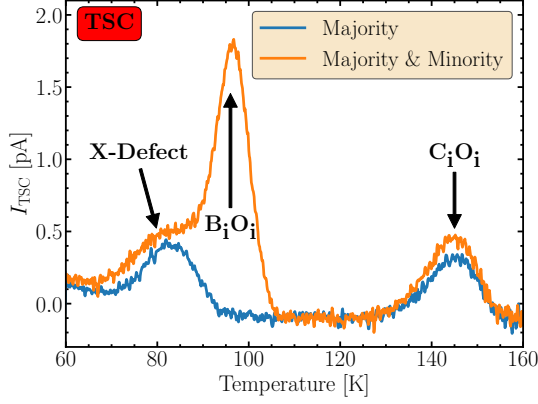


Figure 1: TSC measurements on the electron-irradiated diode. Measurement conditions: a reverse bias (during cooling and heating) of  $U_R = 20$  V, a filling temperature of  $T_{\text{fill}} = 60$  K with either a 0 V bias injection for majority carriers only (blue curve) or a  $-20$  V forward bias (1 mA current) injection for majority and minority carriers (orange curve), with a filling time of  $t_{\text{fill}} = 120$  s and a heating rate of  $11$  K  $\text{min}^{-1}$ .

and a custom LabVIEW software. A closed-cycle liquid Helium cryocooler from ARS [29] was used to control the temperature of the samples from 20 K to 350 K.

### 3. Results and Discussion

Figures 1 and 2 show the results from TSC and DLTS measurements on the electron-irradiated diode. Figure 1 shows the X-Defect as a left shoulder to the  $B_iO_i$  defect peak. By comparing the two filling conditions (only majority in blue, and both majority and minority charge carrier filling in orange), it can be inferred that the X-Defect is a hole trap. Since the  $B_iO_i$  is an electron trap, the X-Defect can be studied without interference from the  $B_iO_i$  peak using a majority carrier only filling measurement (blue line).

The DLTS spectra in Figure 2 obtained on the same diode show similar results. The  $B_iO_i$  has a left shoulder (on the orange curve), labelled as Defect 1. In the following sections, it is shown that Defect 1 corresponds to the X-Defect, and its properties resemble those of the single charged donor level of the di-vacancy  $V_2(+/0)$ .

#### 3.1. Identification of X-Defect in TSC and DLTS

Both, the DLTS and the TSC measurements, identify Defect 1 and the X-Defect as hole traps. Both

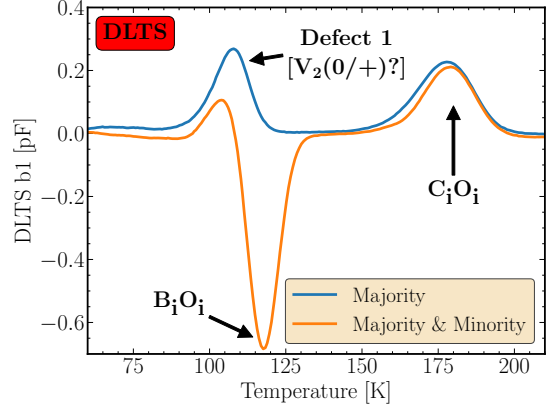


Figure 2: DLTS measurements for the electron-irradiated diode. Measurement conditions: a reverse bias of  $U_R = 10$  V, pulse voltages of  $U_P = 0.6$  V reverse bias for a majority carrier only filling (blue curve) and  $-2$  V forward bias for a majority and minority carrier filling (orange curve), with a pulse duration of  $t_p = 1$  ms, evaluated for time windows  $T_W$  of 20 ms, 200 ms and 2 s. Shown are the spectra obtained from the b1 correlator and  $T_W = 200$  ms.

measurements equally show the  $B_iO_i$  and  $C_iO_i$  defects, as well as one additional defect appearing as a low-temperature shoulder to the  $B_iO_i$  signal (TSC) or a defect distorting the  $B_iO_i$  peak towards its lower temperature tail (DLTS). However, this alone does not suffice to conclude that the X-Defect observed in TSC equals Defect 1, even though the extracted defect parameters are close. It is not straightforward to compare TSC and DLTS spectra, since one is based on current measurements and the other one on capacitance measurements. Furthermore, the temperature at which a defect peak appears is shifted between the two measurement methods and depends strongly on the measurement conditions (e.g. the rate window for DLTS and the heating rate for TSC). Therefore, additional effort is needed to match the results obtained by the two methods. In this study, a simulation of what a TSC spectrum would look like was performed using defect parameters extracted from DLTS measurements to enable a more direct comparison between the two methods. More details about the custom simulation framework is given in Section 3.3.

The result of these simulations, superimposed with a TSC measurement, is shown in Figure 3. The TSC measurement conditions were chosen such that a large fraction of the X-Defect-related traps in the diode were filled. Both the X-Defect and

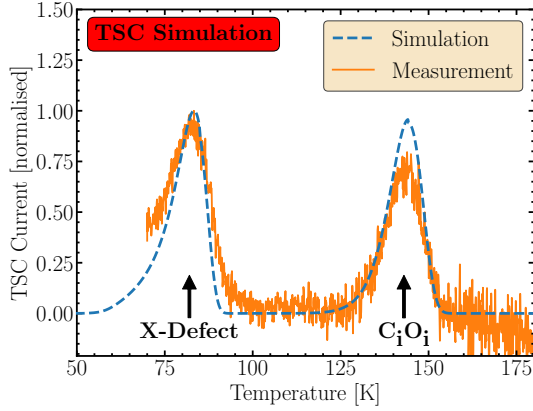


Figure 3: Simulation of a TSC spectrum using defect parameters obtained from DLTS measurements in Figure 2 (blue curve). The TSC measurement was obtained for a reverse bias of 20 V, a filling temperature of 70 K and a filling voltage of 0 V applied for 120 s.

$C_iO_i$  exhibit a strong dependence on the filling temperature  $T_{\text{fill}}$ . This is observed in Figure 4, where under otherwise identical measurement conditions, the electron-irradiated sample was repeatedly measured in TSC, while only varying the filling temperature. Clearly, at higher  $T_{\text{fill}}$ , a larger fraction of the defect-related traps are filled, resulting in higher peak amplitudes.

In Figure 3 it can be seen, that the positions and shapes of both measured peaks, the X-Defect and  $C_iO_i$ , are reproduced by the simulated spectrum. Some discrepancies between the measured and simulated spectra are visible. For one, the absolute currents do not match with the measured ones. The DLTS method measured concentrations about one order of magnitude lower than the TSC method. Therefore, the signal normalised to the X-Defect's amplitude is displayed in the figure. This discrepancy between the two methods could not be explained. Furthermore, the deviation of the amplitude of the  $C_iO_i$  peak, even after the normalisation to the X-Defect's peak, arises from its dependence on the filling temperature and the different filling procedures specific to the DLTS and TSC methods. While in DLTS, filling pulses are applied for each temperature in the temperature ramp, in TSC the filling is done once, at the lowest temperature. Therefore, for centres with temperature dependent capture cross sections like  $C_iO_i$ , the TSC peak will rise as the filling temperature increases. Looking at the spectrum for a filling temperature of 110 K in

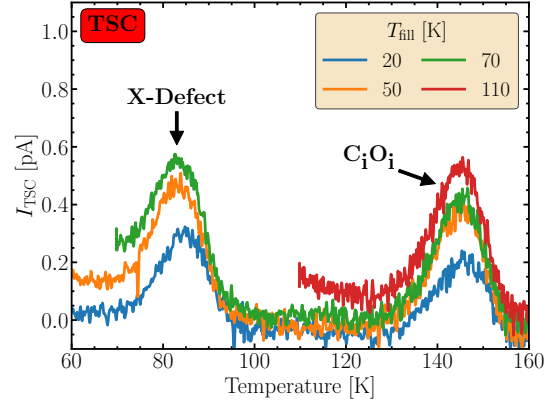


Figure 4: Effect of the filling temperature  $T_{\text{fill}}$  in TSC measurements. Obtained for the electron-irradiated sample with a reverse bias of 20 V and a filling voltage of 0 V for 120 s.

	This work X-Defect	Literature [30] $V_2(+/0)$
Energy Level $E_A$ [eV]	0.186	0.189(3)
Capture Cross Section $\sigma$ [ $\text{cm}^{-2}$ ]	$2.98 \cdot 10^{-16}$	$2.59 \cdot 10^{-16}$
Type of Defect	hole	hole
E-Field Dependent Emission Process	phonon-assisted tunnelling	phonon-assisted tunnelling

Table 1: Comparison of literature values/characteristics for the  $V_2(+/0)$  from Ref. [30] and DLTS measurement results for Defect 1.

Figure 4, it is clear that the filling of  $C_iO_i$  is not yet saturated at  $T_{\text{fill}} = 70$  K.

Most of the observed differences arise from highly idealised assumptions in the simulation of charge carrier emission in  $p-n$  junctions, e.g. constant doping profiles, idealised triangular electric field shapes, no recombination or trapping effects and no charge carrier freeze-out, to name a few. Nonetheless, the simulation gives strong confidence to conclude that both signals, from Defect 1 detected in DLTS and from the X-Defect detected in TSC, belong to the same defect.

### 3.2. Assignment of X-Defect to $V_2(+/0)$

The next step in this study is to demonstrate, that the properties of the X-Defect, now considered synonymous to Defect 1, match those of an already identified radiation-induced defect. Among the multitude of energy levels detected in irradiated Silicon, the donor-charge state of the di-vacancy,

$V_2(+/0)$ , has the closest matching trapping parameters to those of the X-Defect. The defect parameters of the X-Defect and the  $V_2(+/0)$ , as reported by Zangenberg et al. [30], are listed in Table 1.

An exact comparison of the energy level value is difficult, due to the defect's electric field dependent emission process, effectively making  $E_A$  dependent on measurement conditions and the material used. The value shown in Table 1 is for the electron-irradiated sample, a  $10\ \Omega\text{ cm}$   $p$ -type diode, from DLTS measurements with a reverse bias of 10 V and a (reverse) pulse voltage of 0.6 V for a majority carrier filling. The reference article [30] to which the measurement results are compared to, reports their DLTS measurement conditions as  $U_R = 5\text{ V}$  and  $U_P = 1\text{ V}$ , but does not specify the effective doping concentration of their sample. Other studies cite values of 0.191 eV [31] and 0.194 eV [32]. Due to the defect's electric field-dependent emission process, the extrapolated zero-field activation energy  $E_{A,0}$  should be quoted. Nonetheless, a good qualitative match of the activation energies is found. Furthermore, the capture-cross sections differ only slightly, and the differences are well within the measurement uncertainty of 25 % [33]. As  $V_2(+/0)$ , the X-Defect also acts as a hole trap, as shown in Figure 2, where the X-Defect is visible for the majority carrier only filling measurement conditions.

These findings were also presented in earlier works, most recently in Ref. [19]. The final missing information to conclusively match the X-Defect with  $V_2(+/0)$  is the field-dependent emission process. Up to now, it was assumed that the X-Defect follows a Poole-Frenkel mechanism [14]. However, this was never verified and only assumed, since no other emission processes were considered at that time. In the following section, the two relevant emission processes and the required measurements to distinguish them are described.

### 3.2.1. $E$ -Field Dependence of the Emission Rate

Defects can have an electric field strength dependent enhanced emission. This is seen in TSC measurements as a shift of the peak maxima to lower temperatures with increasing applied biases. Not all defects are affected by this, and there are different processes which can cause this behaviour. The two mechanisms relevant for this study are the Poole-Frenkel (PF) effect and phonon-assisted tunnelling (PAT) mechanism. The PF is only applicable for Coulomb centres, defects that are charged after the emission of the charge carrier. This means that the

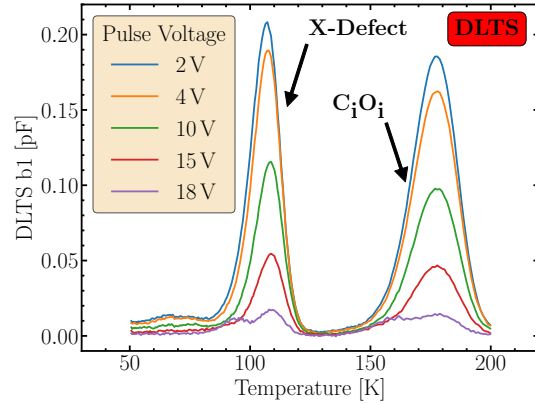


Figure 5: DLTS measurements for different pulse voltages. All measurements were carried out under a reverse bias of 20 V.

ionised defect and the emitted charge carrier interact via the Coulomb interaction and that the applied voltage can lower the emission barrier. Examples of such centres are the Phosphorus and Boron dopants and the  $\text{BiO}_i$  defect. Neutral defects can, however, have an enhanced emission via the PAT mechanism. One way to differentiate between the two processes, when one does not know the charge state of the studied defect, is a method suggested first by Ganichev et al. [34]. PF and PAT differ in the way the charge carrier emission from a defect is enhanced by an electric field strength  $E$ . While the PF shows a  $\sqrt{E}$  dependence of the activation energy, PAT shows an enhanced emission following a  $E^2$  dependence. The activation energy is a precisely measurable quantity and therefore, this method yields a clearly identifiable distinction between the two mechanisms.

To obtain the zero-field activation energy value  $E_{A,0}$  and determine whether the X-Defect exhibits a phonon-assisted tunnelling or Poole-Frenkel enhanced emission, Difference DLTS (DDLTS) measurements were carried out. The DDLTS method works by subtracting two DLTS measurements on a transient-by-transient basis from one another, where they only differ by the applied pulse voltage. Here, pulse voltages only in the reverse bias direction were used, since this enables a study of the X-Defect without interference from the  $\text{BiO}_i$  defect. Different pulse voltages in a diode result in a different depth range of filled defects. By subtracting these measurements from one another, only defects in a small depth range are contributing to the observed signal.

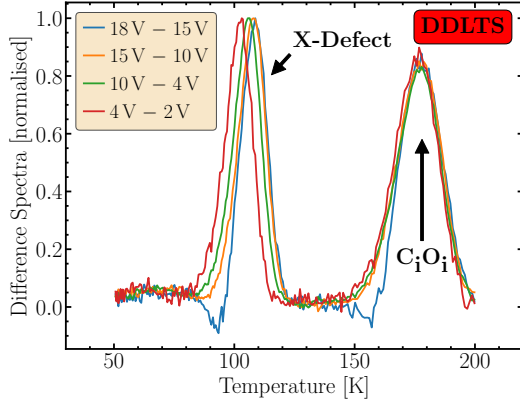


Figure 6: DLTS difference spectra obtained from subtracting the measurements shown in Figure 5 from each other. This results in effectively observing only signals induced by charge carriers under certain electric field strengths.

This, however, also means that they experience only a narrow slice of the full electric field profile in the diode during the emission step.<sup>1</sup> Some exemplary DLTS measurements for different pulse voltages are shown in Figure 5. As can be seen, a smaller pulse voltage results in a larger signal amplitude, due to a larger volume with defects being filled contributing to the signal generation. Figure 6 shows examples of difference spectra obtained after subtracting the pulse measurements from one another, transient by transient. Clear shifts in the positions for the X-Defect peaks are observed, while the  $C_iO_i$  peaks exhibit none, indicating that the X-Defect is subject to a field dependent emission process, while the  $C_iO_i$  is not. For these spectra the standard DLTS analysis with correlator functions is performed to construct an Arrhenius plot, which yields the activation energy. The resulting activation energy versus the applied electric field strength is displayed in Figure 7. The measurement results show that the field strength dependence for the X-Defect activation energy fits well to an  $E^2$  dependence, the expected behaviour for phonon-assisted tunnelling. An approach to fit a  $\sqrt{E}$  dependence, i.e. a PF related dependency, does not result in a good data representation. The least-squares fitting of

$$f(E) = a \cdot E^2 + b \quad (1)$$

to the datapoints results in a zero-field activation energy of  $E_{A,0} = b = (0.1962 \pm 0.0007) \text{ eV}$ . The

<sup>1</sup>This method is instructively illustrated in Ref. [23].

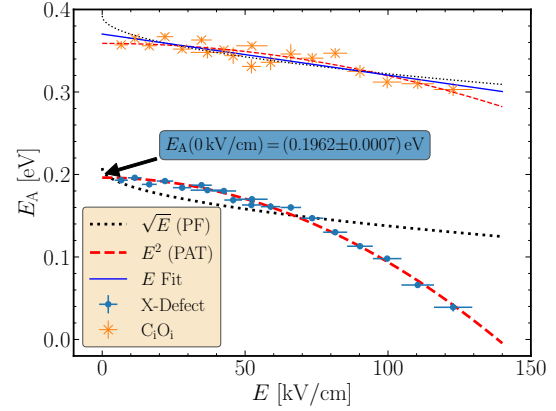


Figure 7: Dependence of the activation energy  $E_A$  on the electric field strength  $E$ . The results for the X-Defect are shown in light blue points, and orange for the  $C_iO_i$ . Functions of the form  $\sqrt{E}$  for the PF (dotted black line),  $E^2$  for the PAT mechanism (dashed red line) and  $E$  linearly (solid blue line, only for  $C_iO_i$ ) are fitted onto the datapoints.

slope parameter for the fit is  $a = (-1.024 \pm 0.014) \cdot 10^{-5} \text{ eV cm kV}^{-1}$ . The reduced  $\chi^2$  is 2.49, indicating a good fit of the PAT  $E^2$  model to the measured data.

For a better visualization of the field dependence, the activation energy data of the X-Defect from Figure 7 is plotted in Figure 8 as a function of  $\sqrt{E}$  and in Figure 9 as a function of  $E^2$ . Evidently, the  $E^2$  dependence results in a straight line as expected for the phonon-assisted tunnelling process.

In Figure 7 it looks like a small change in the activation energy is present for the  $C_iO_i$  defect. However, this is not expected and the observed dependence lies well within the present uncertainties, making a distinction between PF, PAT or a linear dependence not possible. Hence, no conclusions can be drawn about this.

In conclusion, the comparison and good match of all measured characteristics of the X-Defect energy level with the properties of the di-vacancy donor energy level, leads to the conclusion that the X-Defect is indeed the Silicon di-vacancy  $V_2(+/0)$ .

### 3.3. Simulation of Phonon-assisted Tunnelling

To further test the conclusion of the X-Defect being the  $V_2(+/0)$ , hence being subject to the PAT mechanism, TSC measurements of the X-Defect under different bias conditions are compared to simulations using defect parameters obtained from DLTS measurements. In the following, first a description



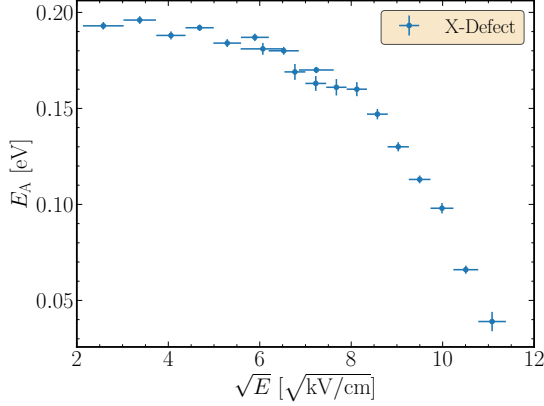


Figure 8: Re-creation of Figure 7, but with the x-axis scaled to  $\sqrt{E}$ . A linear dependence would be expected for defects subject to the PF mechanism.

of the PAT model used in the simulations is given, and then results from the simulations are compared to the measurements.

Phonon-assisted tunnelling causes a change of the emission rate  $e$ , exponentially with the squared electric field strength  $E$

$$\Gamma_{\text{PAT}}(E, T) = \frac{e(E)}{e(0)} = \exp\left(\frac{E^2}{E_c^2}\right), \quad (2)$$

with  $\Gamma_{\text{PAT}}(E, T)$  being the field enhancement factor [34]. Assuming Shockley-Read-Hall emission statistics [35, 36], where

$$e(E) \propto \exp\left(-\frac{E_A^{\text{eff}}(E)}{k_B T}\right), \quad (3)$$

Equation 2 can be reformulated to

$$E_A^{\text{eff}}(E) = E_A(0) - k_B T \left(\frac{E}{E_c}\right)^2, \quad (4)$$

where  $k_B$  is the Boltzmann constant,  $T$  the temperature,  $E$  the electric field strength and  $E_c$  the so-called characteristic field strength

$$E_c = \sqrt{\frac{3m^* \hbar}{q^2 \tau_2^3}}, \quad (5)$$

with  $\hbar$  being the reduced Planck constant,  $q$  the electric charge,  $\tau_2$  the tunnelling time and  $m^*$  the effective mass of the charge carriers [34, 37]. Equation 4 describes the behaviour seen in Figure 7 with

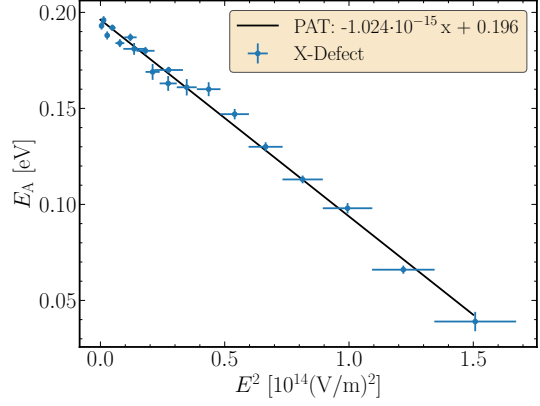


Figure 9: Re-creation of Figure 7, but with the x-axis scaled to  $E^2$ . A linear dependence proves the defect is subject to the PAT mechanism.

Equation 1. Combining this together with Equation 5 yields

$$\tau_2(T) = \left(\frac{-3m^* \hbar a}{q^2 k_B T}\right)^{1/3}. \quad (6)$$

These relations can be used to simulate a PAT-enhanced emission process.

The used simulation software is a fully custom python framework. It is similar to the pyTSC framework used in References [19, 33]. It follows the basic approach to model the thermally stimulated current using the Shockley-Read-Hall emission statistics, with activation energy  $E_A$  and capture cross-section  $\sigma$  as input parameters

$$e(T) = \sigma \cdot v_{\text{th}}(T) \cdot N_c(T) \cdot \exp\left(-\frac{E_A}{k_B T}\right). \quad (7)$$

The thermal velocity  $v_{\text{th}}$  and density of states  $N_c$  are calculated at each temperature step, where the temperature itself is a function of time  $T(t)$ . The sensor thickness is divided into  $n = 1000$  slices, ensuring a sufficiently uniform electric field within each slice. The emission term is then calculated for every temperature step in every slice, while the initialised trap occupancy is updated according to Equation 12. The electric field profile is calculated by assuming an abrupt junction in a planar pad diode [38]. If the applied voltage is smaller than the full depletion voltage  $V_{\text{FD}}$  the field is calculated as

$$E(x) = \begin{cases} \frac{q N_{\text{eff}}}{\epsilon_0 \epsilon_r} (w - x), & x < w, \\ 0, & x \geq w. \end{cases} \quad (8)$$

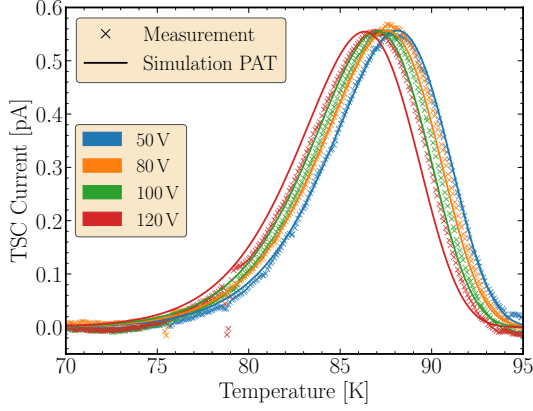


Figure 10: Comparison of TSC measurements on the  $\gamma$ -irradiated diode for different reverse biases with simulated spectra of the X-Defect using the PAT model.

In the case of over-depletion, it is calculated as [22]

$$E(x) = \frac{qN_{\text{eff}}}{\varepsilon_0\varepsilon_r}(w-x) + \frac{V_{\text{tot}} - V_{\text{FD}}}{d}, \quad (9)$$

with  $\varepsilon_0$  being the vacuum permittivity and  $\varepsilon_r$  the relative permittivity of Silicon. The effective doping concentration  $N_{\text{eff}}$  and applied reverse bias  $V_{\text{bias}}$  determine the depletion depth  $w$  with

$$w = \sqrt{\frac{2\varepsilon V_{\text{tot}}}{qN_{\text{eff}}}}, \quad (10)$$

where  $V_{\text{tot}} = V_{\text{bias}} + V_{\text{bi}}$ , and  $V_{\text{bi}}$  being the built-in voltage set to 0.7 V.  $N_{\text{eff}}$  is calculated dynamically for every temperature step and slice, accounting for the emission of trapped charges from defects providing space charge. The emission term is modified by the weighting field for each slice, which in the case of a planar diode corresponds to the inverse of the depletion depth [38]. The given defect concentration is assumed to be homogeneously distributed throughout the sensor bulk, the fraction inside the depleted volume is initialised as fully filled and the remainder as empty. The current is determined by the product of the defect concentration  $N_t$  times the fractional change of the trap occupancy, and summed over all slices and time steps. Taking the product of this with the electric charge  $q$  and depleted volume results in a current with the unit of ampere. The full equation becomes

$$I_{\text{TSC}}(T) = \frac{qA}{2} \sum_{i=1}^n \sum_{\text{Defects}} [e(T)n_t(T)\Gamma(E,T)]\Delta z_i, \quad (11)$$

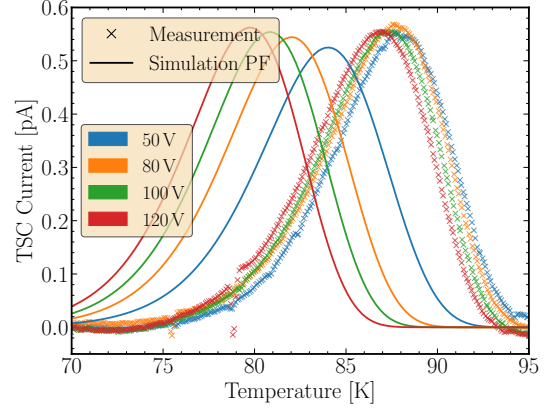


Figure 11: Comparison of TSC measurements on the  $\gamma$ -irradiated diode for different reverse biases with simulated spectra of the X-Defect using the PF model.

where  $\Gamma$  is either Equation 13 for the PF model, Equation 2 for the PAT model or 1 for no field enhancement and  $\Delta z_i$  are the  $n$  slices of the sensor thickness.  $n_t$  is the fraction of defect states occupied, which evolves with an exponential decay over time

$$n_t(T) = N_t(T_0) \exp\left(-\frac{1}{\beta} \int_{T_0}^T e(T) dT\right), \quad (12)$$

with  $\beta = 11 \text{ K min}^{-1}$  being the heating rate.

Two different field enhancement models can be activated for each given defect individually. The PAT model is implemented as described above, with the factor  $\Gamma_{\text{PAT}}(E, T)$  being calculated for each slice and time step and multiplied with the emission term  $e(T)$ . A PF model is also implemented with a  $\Gamma_{\text{PF}}(E, T)$  factor to modify the emission term. It is calculated with the three-dimensional description of the Poole-Frenkel effect from Hartke [39]

$$\Gamma_{\text{PF}}(E, T) = \frac{1}{\gamma^2} [e^{\gamma(\gamma-1)} + 1] + \frac{1}{2}, \quad (13)$$

with

$$\gamma = \frac{q}{k_B T} \sqrt{\frac{qE}{\pi\varepsilon_0\varepsilon_r}}. \quad (14)$$

To validate the implementation of the PF model, a simulation of TSC spectra for the  $\text{B}_i\text{O}_i$  defect was performed and compared to measurements. This is shown and further discussed in Appendix A.

TSC measurements of the  $\gamma$ -irradiated diode for different bias voltages are displayed in Figure 10



and 11 (solid lines). A shift of the X-Defect's peak to lower temperatures with increasing bias is clearly visible. Superimposed on these measurements are the simulated spectra (dotted lines), using the zero-field activation energy from Figure 7 and the capture cross-section obtained from DLTS measurements on the same sample [19]. For this simulation the PAT enhancement model is used. A good, but not perfect match between measurement and simulation is found. At the lower bias voltages, nearly perfect matches are found. At higher biases, i.e. stronger electric fields, the rising edge of the simulated peak is faster compared to the measured one, while the falling edge is not shifted sufficiently to lower temperatures. For all but the highest biases, a good match of the peak maxima is observed.

Figure 11 shows what the effect of the PF would look like for the X-Defect. Clearly, this does not match the measured spectra. The simulated TSC curves assuming a PF effect show peaks at lower temperatures than the measured data. This is in line with the experimental and fitted data shown in Figure 7, where the activation energies from the PF fit are below those of the measurement at the relevant field strengths of the TSC measurements shown in Figure 11 (14 to 22 kV cm<sup>-1</sup>). The observed shift in the measurements do not arise from a PF mechanism.

An overall good agreement between the PAT model and the measurement data is obtained, even though the peak shapes could not be perfectly recreated by the simulation. Additionally, with Figure 11 it can be clearly ruled out that a PF mechanism prevails. In conclusion, these simulations further support the assignment of the X-Defect to the V<sub>2</sub>(+/0).

#### 4. Conclusions

A comprehensive experimental and simulation-based study on identifying the origin of the so-called X-Defect in irradiated *p*-type silicon is presented in this work. This defect is a hole trap and appears as a low-temperature shoulder to the B<sub>i</sub>O<sub>i</sub> defect peak in TSC measurements. Although it was speculated in previous works that the defect could be the singly charged donor state of the di-vacancy V<sub>2</sub>(+/0), it was not identified as such. The observed field strength dependent emission rate was seemingly contradicting the interpretation as the V<sub>2</sub>(+/0) should not be subject to a Poole-Frenkel effect.

This misinterpretation is clarified in this work. By utilising a custom simulation framework it was possible to better link DLTS and TSC measurements in using DLTS-derived parameters to simulate TSC measurements. Furthermore, Difference DLTS measurements were performed to study the dependence of the defect's activation energy on the electric field strength. A clear quadratic dependence was found, providing apparent evidence that the phonon-assisted tunnelling (PAT) mechanism prevails rather than the Poole-Frenkel (PF) effect. This finding is in-line with the previous observation that the X-Defect is not contributing to the effective doping concentration. The identification of PAT as an emission mechanism implies that the X-Defect is electrically neutral in the space charge region, and therefore does not affect  $N_{\text{eff}}$  at ambient temperatures. Furthermore, the measured characteristics of the X-Defect, including apparent activation energy, capture cross-section and emission mechanism, are in good agreement with literature values for the donor charge state of the singly charged di-vacancy, V<sub>2</sub>(+/0). The zero-field activation energy of the X-Defect is determined to be  $E_{A,0} = (0.1962 \pm 0.0007)$  eV.

In conclusion, the defect previously introduced as the X-Defect is indeed the singly charged Silicon di-vacancy, V<sub>2</sub>(+/0).

#### Appendix A. Validation of the PF model

To validate the PF model implementation in the simulation code, TSC measurements for the B<sub>i</sub>O<sub>i</sub> defect were carried out on the  $\gamma$ -irradiated diode at different bias voltages, as the B<sub>i</sub>O<sub>i</sub> defect is known to be subject to the PF effect. The measurements alongside the simulation are shown in Figure A.12 and A.13. An activation energy of 0.27 eV and a capture-cross section of  $1.05 \cdot 10^{-14}$  cm<sup>2</sup> were used as input parameters, taken from Ref. [14]. To obtain the simulated spectra shown in Figure A.12, the emission enhancement factor  $\Gamma_{\text{PF}}$  had to be modified by a factor of 0.97, a modification of 3%. This adjustment is justified by the requirement formulated in Ref. [39]. Hartke states that the PF effect arises from the electrostatic attraction between a singly charged positive ion and an electron under the influence of a uniform electric field. The requirement of a uniform field might not be satisfied for a highly doped, irradiated diode. Therefore, the strength of this attraction is modified. Similar corrections are reported elsewhere [16]. With this modification, the

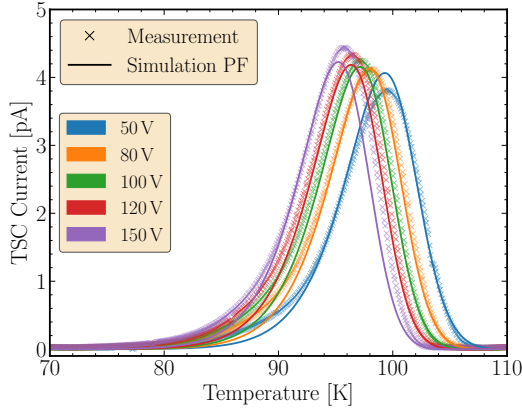


Figure A.12: TSC measurements of the  $\text{BiO}_i$  defect at different bias voltages from the  $\gamma$ -irradiated diode, superimposed with the simulated spectra.

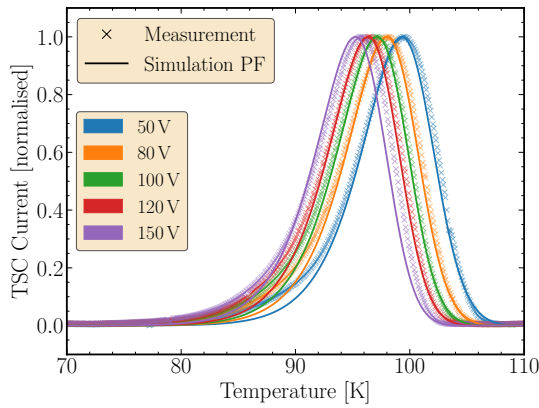


Figure A.13: Figure A.12, but with the currents normalised to each peak's amplitude.

model shows good agreement with the experimental data.

## Acknowledgements

The work was performed partly in the framework of the CERN RD50 and DRD3 collaborations.

Niels Sorgenfrei acknowledges that his work has been sponsored by the Wolfgang Gentner Programme of the German Federal Ministry of Research, Technology and Space (grant no. 13E18CHA).

Ioana Pintilie acknowledges the funding received through the IFA-CERN-RO 07/2024 project.

## Declaration of competing interest

The authors declare that they have no known competing financial interests or personal relationships that could have influenced the work reported in this paper.

## Data availability

The data will be made available on request.

## References

- [1] R. M. FLEMING ET AL., *Defect-driven gain bistability in neutron damaged, silicon bipolar transistors*, 10.1063/1.2731516, Appl. Phys. Lett., 90, 172105 (2007).
- [2] A. JUNKES ET AL., *Annealing study of a bistable cluster defect*, 10.1016/j.nima.2009.08.021, Nucl. Instrum. Methods Phys. Res. A, 612, 525–529 (2010).
- [3] J. COUTINHO ET AL., *Electronic and dynamical properties of the silicon trivacancy*, 10.1103/PhysRevB.86.174101, Phys. Rev. B, 86, 174101 (2012).
- [4] IOANA PINTILIE ET AL., *Second-order generation of point defects in gamma-irradiated float-zone silicon, an explanation for “type inversion”*, 10.1063/1.1564869, Appl. Phys. Lett., 82, 2169–2171 (2003).
- [5] G. D. WATKINS ET AL., *Defects in Irradiated Silicon: Electron Paramagnetic Resonance and Electron-Nuclear Double Resonance of the Si-E Center*, 10.1103/PhysRev.134.A1359, Phys. Rev., 134, A1359–A1377 (1964).
- [6] P. M. MOONEY ET AL., *Defects energy levels in boron-doped silicon irradiated with 1-MeV electrons*, 10.1103/PhysRevB.15.3836, Phys. Rev. B, 15, 3836–3843 (1977).
- [7] C. BESLEAGA ET AL., *Bistability of the  $\text{BiO}_i$  complex and its implications on evaluating the “acceptor removal” process in p-type silicon*, 10.1016/j.nima.2021.165809, Nucl. Instrum. Methods Phys. Res. A, 1017, 165809 (2021).
- [8] IOANA PINTILIE ET AL., *Stable radiation-induced donor generation and its influence on the radiation tolerance of silicon diodes*, 10.1016/j.nima.2005.10.013, Nucl. Instrum. Methods Phys. Res. A, 556, 197–208 (2006).
- [9] IOANA PINTILIE ET AL., *Cluster related hole traps with enhanced-field-emission—the source for long term annealing in hadron irradiated Si diodes*, 10.1063/1.2832646, Appl. Phys. Lett., 92, 24101 (2008).
- [10] D. V. MAKHOV ET AL., *Stable Fourfold Configurations for Small Vacancy Clusters in Silicon from ab initio Calculations*, 10.1103/PhysRevLett.92.255504, Phys. Rev. Lett., 92, 255504 (2004).
- [11] MICHAEL MOLL, *Acceptor removal - Displacement damage effects involving the shallow acceptor doping of p-type silicon devices*, 10.22323/1.373.0027, PoS(Vertex2019), 27 (2020).
- [12] VALENTINA SOLA ET AL., *The first batch of compensated LGAD sensors*, 10.1016/j.nima.2024.169453, Nucl. Instrum. Methods Phys. Res. A, 1064, 169453 (2024).
- [13] M. FERRERO ET AL., *Radiation resistant LGAD design*, 10.1016/j.nima.2018.11.121, Nucl. Instrum. Methods Phys. Res. A, 919, 16–26 (2019).

- [14] CHUAN LIAO ET AL., *The Boron–Oxygen ( $B_iO_i$ ) Defect Complex Induced by Irradiation With 23 GeV Protons in p-Type Epitaxial Silicon Diodes*, 10.1109/TNS.2022.3148030, IEEE Trans. Nucl. Sci., 69, 3, 576–586 (2022).
- [15] ANJA HIMMERLICH ET AL., *Defect characterization studies on irradiated boron-doped silicon pad diodes and Low Gain Avalanche Detectors*, 10.1016/j.nima.2022.167977, Nucl. Instrum. Methods Phys. Res. A, 1048, 167977 (2023).
- [16] CHUAN LIAO ET AL., *Investigation of the Boron removal effect induced by 5.5 MeV electrons on highly doped EPI- and Cz-silicon*, 10.1016/j.nima.2023.168559, Nucl. Instrum. Methods Phys. Res. A, 1056, 168559 (2023).
- [17] CHUAN LIAO, *Boron Removal Effect in p-type Silicon Sensors*, ediss.sub.uni-hamburg.de/handle/ediss/10480, PhD Thesis, University of Hamburg, Germany (2023).
- [18] JACOB FRENKEL, *On Pre-Breakdown Phenomena in Insulators and Electronic Semi-Conductors*, 10.1103/PhysRev.54.647, Phys. Rev., 54, 647–648 (1938).
- [19] ANJA HIMMERLICH ET AL., *Defects and acceptor removal in  $^{60}\text{Co}$   $\gamma$ -irradiated p-type silicon*, 10.1016/j.nima.2025.170886, Nucl. Instrum. Methods Phys. Res. A, 1081, 170886 (2025).
- [20] MICHAEL MOLL, *Radiation Damage in Silicon Particle Detectors - microscopic defects and macroscopic properties*, 10.3204/PUBDB-2016-02525, Doctoral thesis, University of Hamburg, Chapters 4.4 & 4.5 (1999).
- [21] IOANA PINTILIE ET AL., *Thermally stimulated current method applied on diodes with high concentration of deep trapping levels*, 10.1063/1.1335852, Appl. Phys. Lett., 78, 550–552 (2001).
- [22] ANDREI NITESCU ET AL., *Bistable Boron-Related Defect Associated with the Acceptor Removal Process in Irradiated p-Type Silicon—Electronic Properties of Configurational Transformations*, 10.3390/s23125725, Sensors, 23, 5725 (2023).
- [23] NIELS SORGENFREI ET AL., *Hunting the X-Defect*, indico.cern.ch/event/1507215/contributions/6539534/, Talk at the 3rd DRD3 Workshop in Amsterdam, Slides 11-12 (2025).
- [24] CİS FORSCHUNGSINSTITUT FÜR MIKROSENSORIK GMBH, <https://www.cismst.de/en/welcome/>, Accessed August 2025 (2025).
- [25] BELARIUSSIAN STATE UNIVERSITY, <https://bsu.by/en/>, 5.5 MeV electron irradiation (2025).
- [26] RUĐER BOŠKOVIĆ INSTITUTE, <https://www.irb.hr/eng/>,  $^{60}\text{Co}$ - $\gamma$  irradiation (2025).
- [27] ELENA M. DONEGANI ET AL., *Study of point- and cluster-defects in radiation-damaged silicon*, <https://doi.org/10.1016/j.nima.2018.04.051>, Nucl. Instrum. Methods Phys. Res. A, 898, 15–23 (2018).
- [28] PHYSTECH, <http://www.phystech.de/products/dlts/dlts.htm> (2025).
- [29] ADVANCED RESEARCH SYSTEMS, <https://www.arscryo.com/>, Accessed August 2025 (2025).
- [30] NIKOLAJ ZANGENBERG ET AL., *On-line DLTS investigations of vacancy related defects in low-temperature electron irradiated, boron-doped Si*, 10.1007/s00339-003-2358-3, Appl. Phys. A, 80, 1081–1086 (2005).
- [31] NIKOLAJ ZANGENBERG ET AL., *On-line DLTS investigations of the mono- and di-vacancy in p-type silicon after low temperature electron irradiation*, 10.1016/S0168-583X(01)00876-X, Nucl. Instrum. Methods Phys. Res. B, 186, 1–4, 71–77 (2002).
- [32] ANDERS HALLÉN ET AL., *Lifetime in proton irradiated silicon*, 10.1063/1.361816, J. Appl. Phys., 79, 3906–3914 (1996).
- [33] NIELS SORGENFREI ET AL., *Characterisation of Crystalline Defects in 4H Silicon Carbide using DLTS and TSC*, 10.1088/1748-0221/20/07/C07006, J. Inst., 20, C07006 (2025).
- [34] S. D. GANICHEV ET AL., *Distinction between the Poole-Frenkel and tunneling models of electric-field-stimulated carrier emission from deep levels in semiconductors*, 10.1103/PhysRevB.61.10361, Phys. Rev. B, 61, 10361–10365 (2000).
- [35] W. SHOCKLEY AND W. T. READ, JR., *Statistics of the Recombinations of Holes and Electrons*, 10.1103/PhysRev.87.835, Phys. Rev., 87, 835–842 (1952).
- [36] R. N. HALL, *Electron-Hole Recombination in Germanium*, 10.1103/PhysRev.87.387, Phys. Rev., 87, 387 (1952).
- [37] S. D. GANICHEV ET AL., *Deep impurity-center ionization by far-infrared radiation*, 10.1134/1.1130157, Phys. Solid State, 39, 1703–1726 (1997).
- [38] S. M. SZE, KWOK K. NG, *Physics of Semiconductor Devices*, 10.1002/0470068329, 3rd Edition, Chapter 2, Equation 11, John Wiley & Sons, Inc. (2006).
- [39] J. L. HARTKE, *The Three-Dimensional Poole-Frenkel Effect*, 10.1063/1.1655871, J. Appl. Phys., 39, 4871–4873 (1986).